

OPEN ACCESS

In-Plane Ordering of Li-Intercalated Turbostratic Graphite for the Negative Electrode of High-Power Long-Life Li-Ion Batteries

To cite this article: Hiroyuki Fujimoto *et al* 2023 *J. Electrochem. Soc.* **170** 060534

View the [article online](#) for updates and enhancements.

You may also like

- [High-responsivity turbostratic stacked graphene photodetectors using enhanced photogating](#)
Masaaki Shimatani, Naoki Yamada, Shoichiro Fukushima et al.
- [Resonance Raman spectroscopy of twisted interfaces in turbostratic multilayer graphene](#)
A Mohapatra, S Poudyal, M S Ramachandra Rao et al.
- [Computational analysis of electrical conduction in hybrid nanomaterials with embedded non-penetrating conductive particles](#)
Jizhe Cai and Mohammad Naraghi



Your Lab in a Box!

The PAT-Tester-i-16: All you need for Battery Material Testing.

- ✓ All-in-One Solution with integrated Temperature Chamber!
- ✓ Cableless Connection for Battery Test Cells!
- ✓ Fully featured Multichannel Potentiostat / Galvanostat / EIS!

www.el-cell.com +49 40 79012-734 sales@el-cell.com

EL-CELL[®]
electrochemical test equipment





In-Plane Ordering of Li-Intercalated Turbostratic Graphite for the Negative Electrode of High-Power Long-Life Li-Ion Batteries

Hiroyuki Fujimoto,^{1,✉} Keiji Shimoda,¹ Miwa Murakami,¹ Hisao Kiuchi,¹ Shigeharu Takagi,¹ Gentaro Kano,¹ Mitsuo Kawasaki,¹ Zempachi Ogumi,¹ and Takeshi Abe²

¹Office of Society-Academia Collaboration for Innovation, Kyoto University, Gokasho, Uji, Kyoto 611-0011, Japan

²Graduate School of Global Environmental Studies, Kyoto University, Katsura, Nishikyo-ku, Kyoto 615-8510, Japan

Turbostratic carbon graphitized at ca. 2000 °C exhibits low discharge capacity but excellent pulse charge/discharge characteristics and long cycle performance. In this study, to clarify the charge/discharge mechanism, the intercalation process of Li into turbostratic graphite was investigated by operando synchrotron X-ray diffraction and ⁷Li-NMR spectroscopy. The dataset obtained from both methods was synchronously analyzed by treating it as a function of the LiC_x composition estimated from the charge/discharge curves. It was found that both the synchrotron X-ray diffraction profile and ⁷Li-NMR spectrum dynamically changed in conjunction with the composition and the LiC₉-type and LiC₆-type in-plane structures formed in turbostratic graphite, as in the case of natural graphite when Li ions intercalate. The domain formed by these in-plane structures was a short-range ordered structure that changed depending on the misorientation angle between the two adjacent graphene sheets, and a stage structure with a periodic distance in the *c*-axis direction did not form, as in the case of natural graphite.

© 2023 The Author(s). Published on behalf of The Electrochemical Society by IOP Publishing Limited. This is an open access article distributed under the terms of the Creative Commons Attribution Non-Commercial No Derivatives 4.0 License (CC BY-NC-ND, <http://creativecommons.org/licenses/by-nc-nd/4.0/>), which permits non-commercial reuse, distribution, and reproduction in any medium, provided the original work is not changed in any way and is properly cited. For permission for commercial reuse, please email: permissions@iopublishing.org. [DOI: [10.1149/1945-7111/acde63](https://doi.org/10.1149/1945-7111/acde63)]



Manuscript received May 4, 2023. Published June 22, 2023.

About 30 years have passed since the Li-ion battery with carbon as the negative electrode was commercialized. During this period, the negative electrode characteristics of most carbon materials have been investigated, and they can be roughly classified into two types based on the charge/discharge curve profiles: hard carbon materials (non-graphitizable carbon materials) and graphitizable carbon materials. The former was first reported by Sonobe et al.¹ Hard carbon materials have been continuously studied because they exhibit higher discharge capacity than the theoretical capacity of 372 Ah kg⁻¹ estimated from the composition of stage-1 li-graphite intercalation (LiC₆).^{2–6} The latter can be further systematically classified into three types because the changes of the electrochemical characteristics depend on the heat-treatment temperature. The first group consists of carbon materials prepared by heat treatment of carbonaceous precursors below ca. 1000 °C, such as raw meso-carbon microbeads and condensed polynuclear aromatic compounds.^{7–10} Their capacities are also higher than 372 Ah kg⁻¹. However, their cycle performance is poor and their initial coulombic efficiencies are less than ca. 80%. For this reason, their electrochemical characteristics are now hardly investigated. The second group is natural graphite or artificial graphite with high crystallinity graphitized above ca. 2500 °C. In general, these graphite materials show excellent cycle performance, high capacities comparable with the theoretical capacity of 372 Ah kg⁻¹, and coulombic efficiencies of higher than 90%. Therefore, graphite is commercially used as the negative electrode of most Li-ion batteries. The third group is turbostratic graphite materials heat treated between 1100 and 2500 °C. In this temperature range, the discharge capacity shows a minimum value at ca. 1800 °C–2000 °C. Very few researchers have therefore studied the characteristics of these carbon materials. Tatsumi et al.¹¹ reported that these materials have a linear relationship between the degree of graphitization and discharge capacity, and Zheng and Dahn reported that the turbostratic graphite with high disorder parameters exhibits the low capacity.^{12,13}

In conventional studies and development of carbon negative electrodes, improvement of the capacity, initial coulombic efficiency, and cyclability has been emphasized from the viewpoint of their use in mobile electronic devices. However, since 2000, the

research activities of large-scale Li-ion batteries have increased for application to electric vehicles. Such applications require a carbon material with high power density and long-life performance. Ozaki found that turbostratic graphite materials heat treated at 1800 °C–2400 °C show excellent characteristics, such as high-rate charge/discharge performance and cyclability, and they called them “ICOKE.”^{14–17} They assembled a 5-Ah-class large-scale battery using ICOKE as the negative electrode and evaluated the life performance by pulse charge/discharge cycling at 40 °C. The pulse cycle test exceeded 240,000 cycles, and 93% of the capacity and 92% of the power were retained.¹⁵ Focusing on these excellent characteristics, Osaka Gas Chemical Co., Ltd. succeeded in commercializing this material under the trademark GRAMAX. In general, heat treatment of carbon materials in the temperature range 1800 °C–2400 °C results in turbostratic graphite with random stacking of graphene layers along the *c*-axis direction, and adjacent graphene layers do not form AB-stacking structures as in graphite. In the case of natural graphite with the AB-stacking structure, intercalation causes slipping from the AB-stacking structure to the AA-stacking structure to form a LiC₉-type in-plane structure up to stage 3 with composition of LiC₂₇, and then a LiC₆-type in-plane structure is formed in stage 2 (LiC₁₂) and stage 1 (LiC₆).^{18–21} However, in the case of turbostratic graphite, because the adjacent graphene layers are randomly stacked along the *c*-axis direction, it is not clear whether similar graphene slipping in graphite causes formation of a LiC₉-type or a LiC₆-type in-plane structure based on AA-type stacking. In this study, synchronous operando analysis combining synchrotron X-ray diffraction (SXD) and ⁷Li-NMR spectroscopy was performed to investigate the in-plane structure of Li-intercalated turbostratic graphite graphitized at ca. 2000 °C, which shows high power and excellent cyclability.

Experimental

Operando analysis.—Intercalation/deintercalation of Li ions into/from turbostratic graphite was investigated by operando SXD and ⁷Li-NMR spectroscopy. Because the measurement principles of the two methods are different, it is not possible to simultaneously perform the measurements. Therefore, each operando measurement was independently performed using the same graphite electrode under identical charge/discharge conditions and the successively obtained spectral datasets were synchronously analyzed with the

[✉]E-mail: fujimoto.hiroyuki.5n@kyoto-u.ac.jp

charge/discharge curves, the LiC_x compositions calculated from the capacity, Q and the differential capacity curves for the potential, V ($V\text{-d}Q/\text{d}V$).^{22,23} Turbostratic graphite (GRAMAX) and natural graphite (OMAC) manufactured by Osaka Gas Chemical Co., Ltd. in Japan, were used as the working electrode. The physical parameters of both samples are listed in Table 1. The graphite negative electrodes were fabricated by coating on copper foil using an SBR binder. Lithium metal and $1\text{ mol}\cdot\text{dm}^{-3}$ LiPF_6 -ethylene carbonate/ethyl methyl carbonate (3:7) (Kishida Chemical Co., Ltd. Japan) were used as the counter electrode and electrolyte, respectively.

Operando SXD measurement.—A three-layer aluminum-laminated half cell (electrode area $20\text{ mm} \times 20\text{ mm}$) composed of a graphite negative electrode, a separator, and a Li-foil positive electrode was assembled according to a previous report.^{22,23} The SXD measurements were performed during the charge/discharge cycle in the range $0.01\text{--}2.5\text{ V}$ at 0.1 CA current rate at beamline BL28XU of Super Photon ring-8 (SPring-8), Japan. A SXD diffraction profile was acquired every 10 s , and ca. 7200 profiles were obtained during the charge/discharge process. The detailed conditions of the operando measurement have already been reported. The wavelength and size of the X-ray source were 0.049592 nm (25 keV), and $0.2\text{ mm} \times 0.5\text{ mm}$, respectively.

Operando ^7Li -NMR measurement.—A three-layer laminated cell composed of a graphite electrode ($5\text{ mm} \times 15\text{ mm}$), a separator, and a Li electrode was assembled according to a previous study.²³ A polyethylene terephthalate film was used as the laminating material. The ^7Li -NMR operando measurements were performed with a DD2 600 spectrometer (Agilent Technologies, Inc.) using a probe containing a solenoid coil with a diameter of 10 mm under the same charge/discharge conditions as the SXD measurements. The spectra were measured at 60 s intervals, and approximately 600 spectra were acquired in 10 h . The ^7Li chemical shift was relative to 1 M LiCl solution at 0.0 ppm .

In the above-mentioned cell, lithium metal was used as the counter and reference electrodes, so the graphite electrode was positive in this cell system. However, the terms “charge” for Li intercalation and “discharge” for Li deintercalation will be used in connection with a practical rechargeable lithium battery.

Synchronous operando analysis.—By the above method, datasets of 7200 continuous SXD profiles and 1200 continuous ^7Li -NMR spectra were obtained during charge/discharge cycling. These operando datasets were synchronously analyzed in conjunction with the charge/discharge curves, $V\text{-d}Q/\text{d}V$ curves, and the LiC_x compositions using the analysis software “Profile Chaser” developed in a previous study.²³

Results and Discussion

Charge/discharge curves and their differential curves.—The charge/discharge curves of cycles 1–3 and their $V\text{-d}Q/\text{d}V$ curves for GRAMAX are shown in Fig. 1. In the deintercalation process, the overpotential of each cycle was almost the same, and the $V\text{-d}Q/\text{d}V$ curves almost overlapped. By contrast, the overpotential in the intercalation process decreased with increasing cycle number, and the peak of the $V\text{-d}Q/\text{d}V$ curve also shifted to the higher potential side. This indicates that the intercalation reaction proceeded more smoothly as the number of cycles increased, suggesting that the structure of the turbostratic graphite changed. Operando analysis was performed focusing on these points.

Dynamic changes in the ^7Li -NMR spectrum and SXD profiles during intercalation in the first cycle.—The dynamic changes of the ^7Li -NMR spectrum and 100 and 002 diffractions of GRAMAX during the intercalation process in the first cycle are shown in Fig. 2. For comparison, the dynamic changes of natural graphite are shown

in Fig. 3. There are three peaks in the ^7Li -NMR spectra of both GRAMAX and natural graphite: peak I ($\delta = 0\text{--}25\text{ ppm}$), peak II ($\delta = 35\text{--}50\text{ ppm}$), and peak III ($\delta = 70\text{--}100\text{ ppm}$). Letellier and co-workers^{24,25} reported that peaks I and II are derived from the LiC_9 - and LiC_6 -type in-plane structures, respectively. Based on their results, it is concluded that LiC_9 - and LiC_6 -type in-plane structures are formed even in turbostratic graphite in the same manner as in natural graphite. However, comparing the two carbon materials, peaks I and II are broader for GRAMAX. In the case of natural graphite, at $\text{C/Li} = 21.2$, the LiC_6 -type structure formed almost at the same time as the disappearance of the LiC_9 -type structure. By contrast, in the case of GRAMAX, these two types of structures coexisted until almost the end of intercalation, and it is presumed that there is a slight difference between GRAMAX and natural graphite regarding these in-plane structures. Peak III is a satellite peak of peak II. In the case of natural graphite, we previously reported that the satellite peak shifts from $\delta = 80\text{ ppm}$ to $\delta = 90\text{ ppm}$ near $\text{C/Li} = 9.5$ during the transition from stage 2 to stage 1 as shown in Fig. 3A, and we concluded that the peak reflects the difference in the stage structures.²³ For GRAMAX, this signal was very weak and could only be observed in the high Li ion concentration range of $\text{C/Li} < 13.4$.

In the SXD profiles of both GRAMAX and natural graphite, there were large changes in the positions and intensities of the diffraction lines near $\text{C/Li} = 21.2$ for the 100 and 002 diffractions. We previously reported that for natural graphite, the transition from the LiC_9 -type in-plane structure to the LiC_6 -type structure occurs in the vicinity of this composition.^{22,23} At the same time, peak II derived from the LiC_6 -type structure with this composition appeared in the ^7Li -NMR spectrum. Therefore, in the case of GRAMAX, it is concluded that the LiC_9 -type structure mainly formed for $\text{C/Li} > 21.2$ and the LiC_6 -type structure mainly formed for $\text{C/Li} < 21.2$. However, the 110 and 001 diffraction lines corresponding to stage 1 observed for natural graphite were not observed at $d = 0.216$ and 0.37 nm for GRAMAX.

For GRAMAX, the positions and intensities of the 100 and 002 diffraction lines clearly changed again near $\text{C/Li} = 10.9$. Both diffraction lines shifted in the larger d direction, causing broadening. d_{100} is geometrically related to the $\text{C}=\text{C}$ bond length ($d_{\text{C}=\text{C}}$) in the six-membered carbon ring by

$$d_{\text{C}=\text{C}} = 2/3d_{100} \quad [1]$$

This indicates that the six-membered-ring size increases as the Li-ion concentration increases. An increase in the d_{002} value also indicates that the interlayers between two adjacent graphene layers expand in the c -axis direction. That is, the volume expands in the a -, b -, and c -axis directions owing to further insertion of Li ions. An increase in the Li-ion concentration causes crystallite expansion, a slight weakening of the van der Waals force between adjacent graphene layers, and a smaller misorientation angle, allowing more Li ions to be stored.

Dynamic changes in the ^7Li -NMR spectrum and SXD profiles in the second cycle.—The dynamic changes of the ^7Li -NMR spectrum and 100 and 002 diffraction lines of GRAMAX in the second cycle are shown in Fig. 4. All of the profiles changed in conjunction with each other, as in the first cycle. However, the compositions at which the clear profile changes occurred were slightly different from those in the first cycle. To investigate the dynamic behavior in the second cycle in more detail, the diffraction profiles obtained at 1% intervals of state of charge (SOC) in the first and second cycles were superimposed for comparison with those of the natural graphite profiles in the second cycle. The results are shown in Figs. 5A–5C, respectively. By comparing Figs. 5B and 5C, the behavior of the profile change differed between the first and second cycles for both 100 and 002 diffraction. In particular, the initial 002 diffraction at the start of charging in the first cycle was a single peak, but a doublet peak was observed at the start of the

Table I. Physical parameters of pristine materials supplied by Osaka Gas Chemical Co., Ltd. All the parameters were supplied by Osaka Gas Chemical Co., Ltd.

Sample	D50/ μm	Specific surface area/ m^2g^{-1}	Lattice constant, a_0/nm	Lattice constant, c_0/nm	Degree of graphitization $P_1/\%$	Average misorientation, $\phi/^\circ$
OMAC	18.25	3.0	0.2461	0.671	—	—
GRAMAX	12	2.3	—	0.678	0.52	2.51

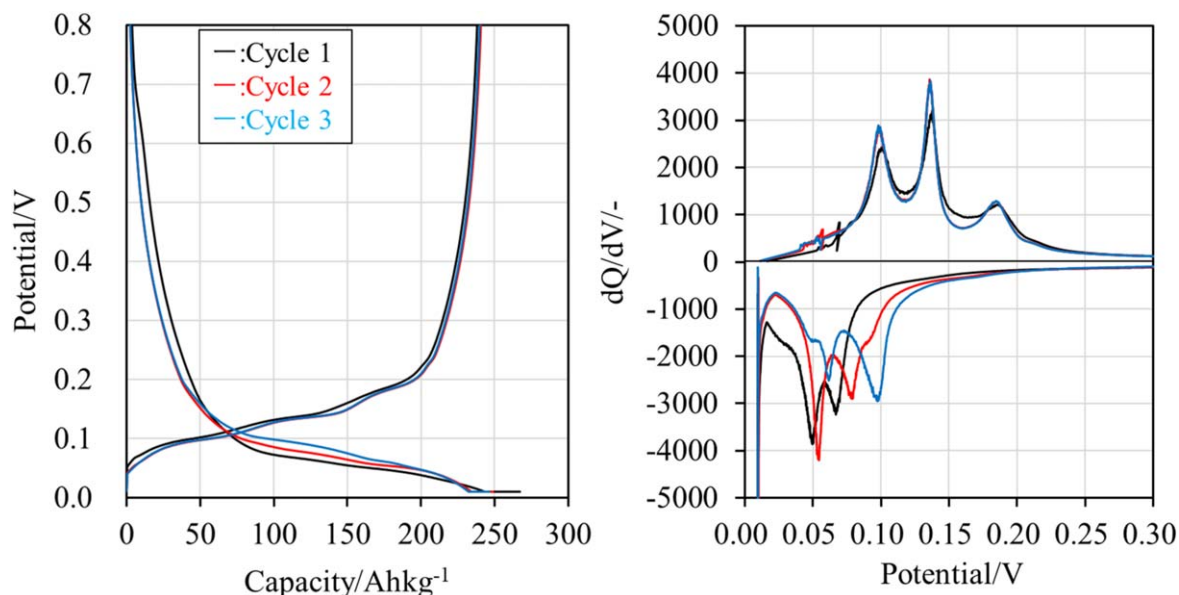


Figure 1. Charge/discharge curves (left) and their differential curves (right).

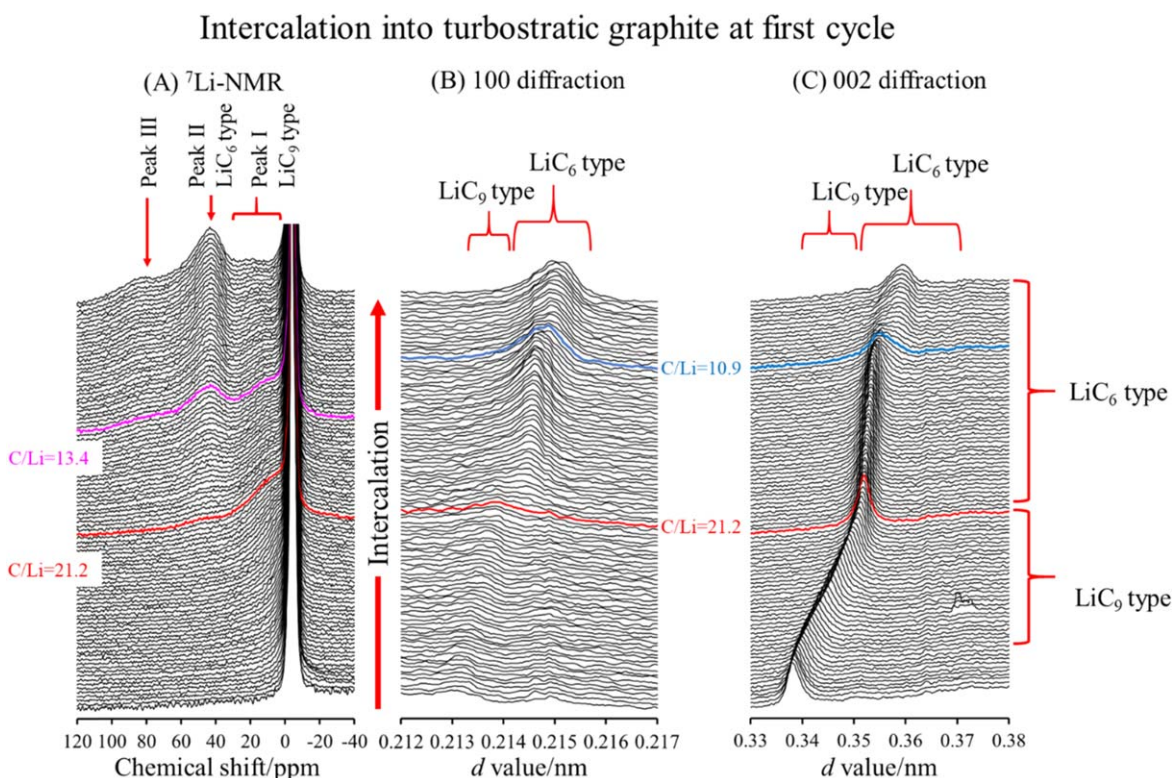


Figure 2. Dynamic changes of the ⁷Li-NMR spectrum and 100 and 002 diffraction profiles of GRAMAX during the charge (intercalation) process in the first cycle.

second cycle. That is, an irreversible structural change partially occurred in the charge/discharge process of the first cycle. There are several possibilities for why this occurred. The first possibility is that some Li ions remained in the layers and the structure could not be restored because the coulombic efficiency in the first cycle was 91.4%. The second possibility is that the expansion/contraction in the *a*-, *b*-, and *c*-axis directions due to intercalation/deintercalation of Li ions in the first cycle caused slight displacement in the misorientation angle between two adjacent graphene layers, and an irreversible change occurred in the random layer structure. This

would be the reason why the overpotential during the charge process decreased as the number of cycles increased.

Dynamic changes in the ⁷Li-NMR spectrum and SXD profiles during deintercalation in the second cycle.—The dynamic changes of the ⁷Li-NMR spectrum and 100 and 002 diffraction lines of GRAMAX during the discharge process of the second cycle are shown in Fig. 6. In the 100 and 002 diffraction lines, there were large changes in the positions and intensities of the diffractions near C/Li = 55, 20, and 10, as in the case of Li intercalation. In the

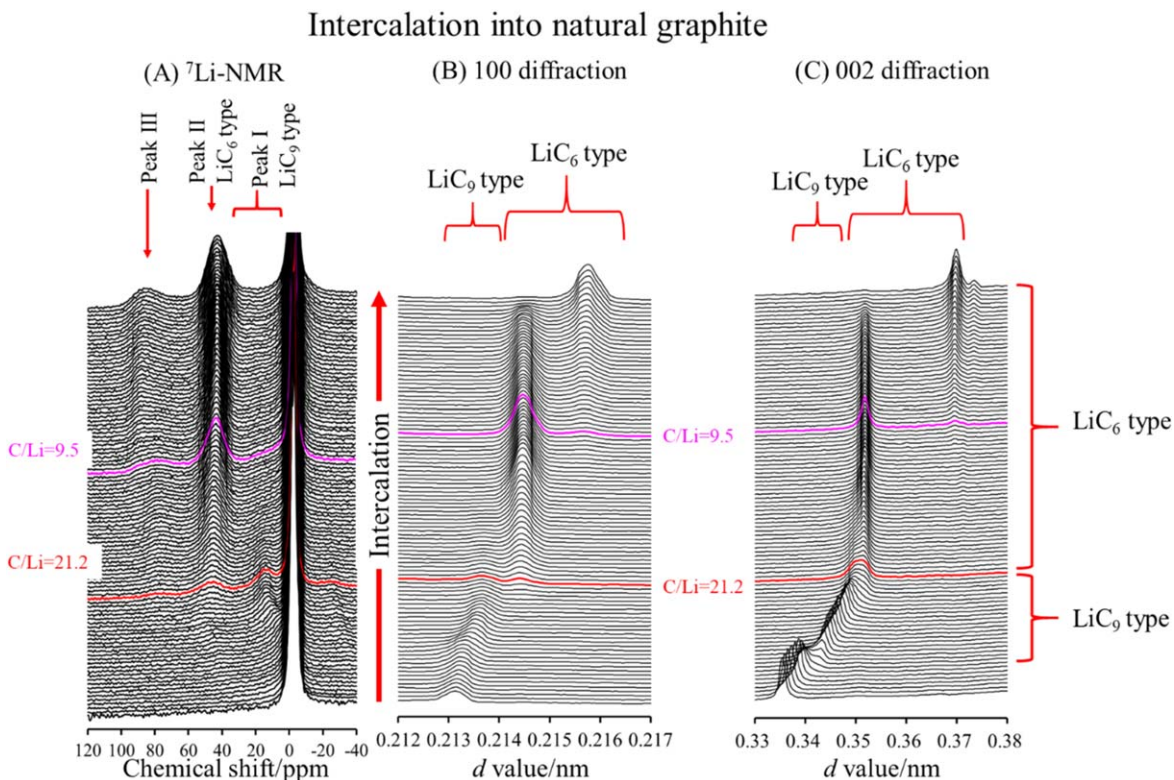


Figure 3. Dynamic changes of the ^7Li -NMR spectrum and 100 and 002 diffraction profiles of natural graphite during the charge (intercalation) process.

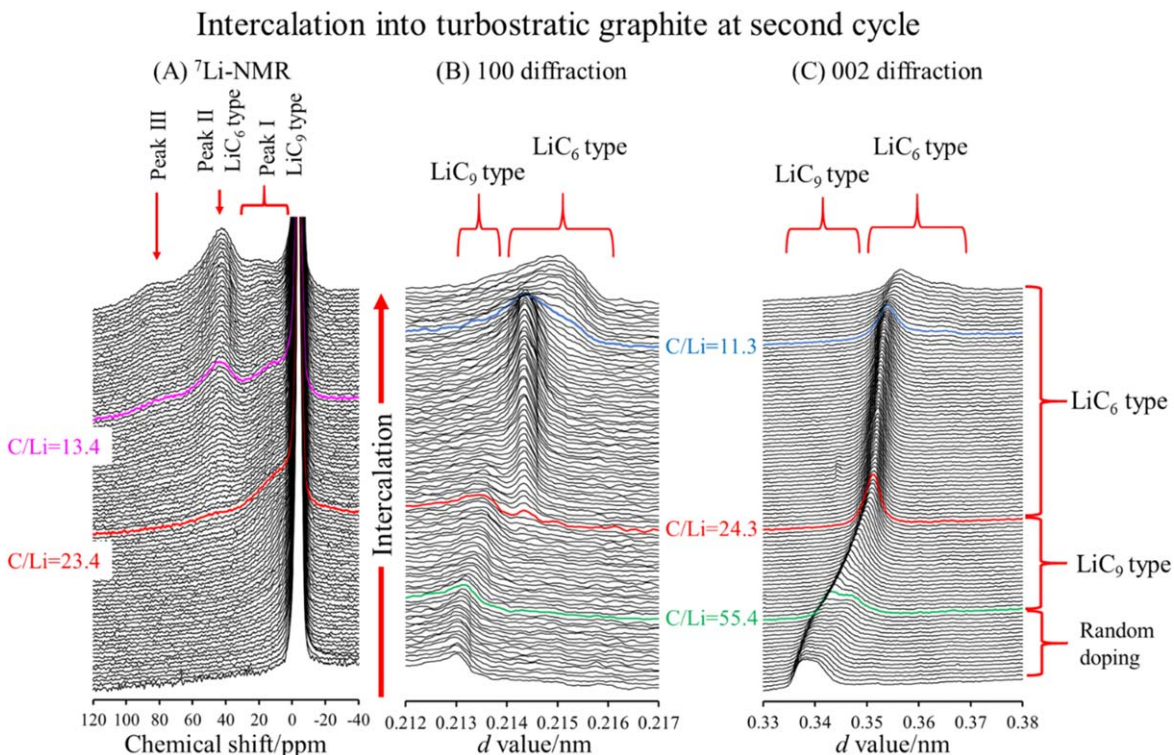


Figure 4. Dynamic changes of the ^7Li -NMR spectrum and 100 and 002 diffraction profiles of GRAMAX during the charge (intercalation) process in the second cycle.

vicinity of $\text{C/Li} = 10$, both the 100 and 002 diffraction lines sharpened while shifting in the smaller d value direction. The misorientation angle, which decreased with expansion of the crystallite during the charge process, increased again during the

deintercalation process, indicating that the crystallite contracted. In the ^7Li -NMR spectrum, a change in the signal occurred at $\text{C/Li} = 18.9$, indicating the transition from the LiC_6 -type structure to the LiC_9 -type structure. In conjunction with this change, a transition

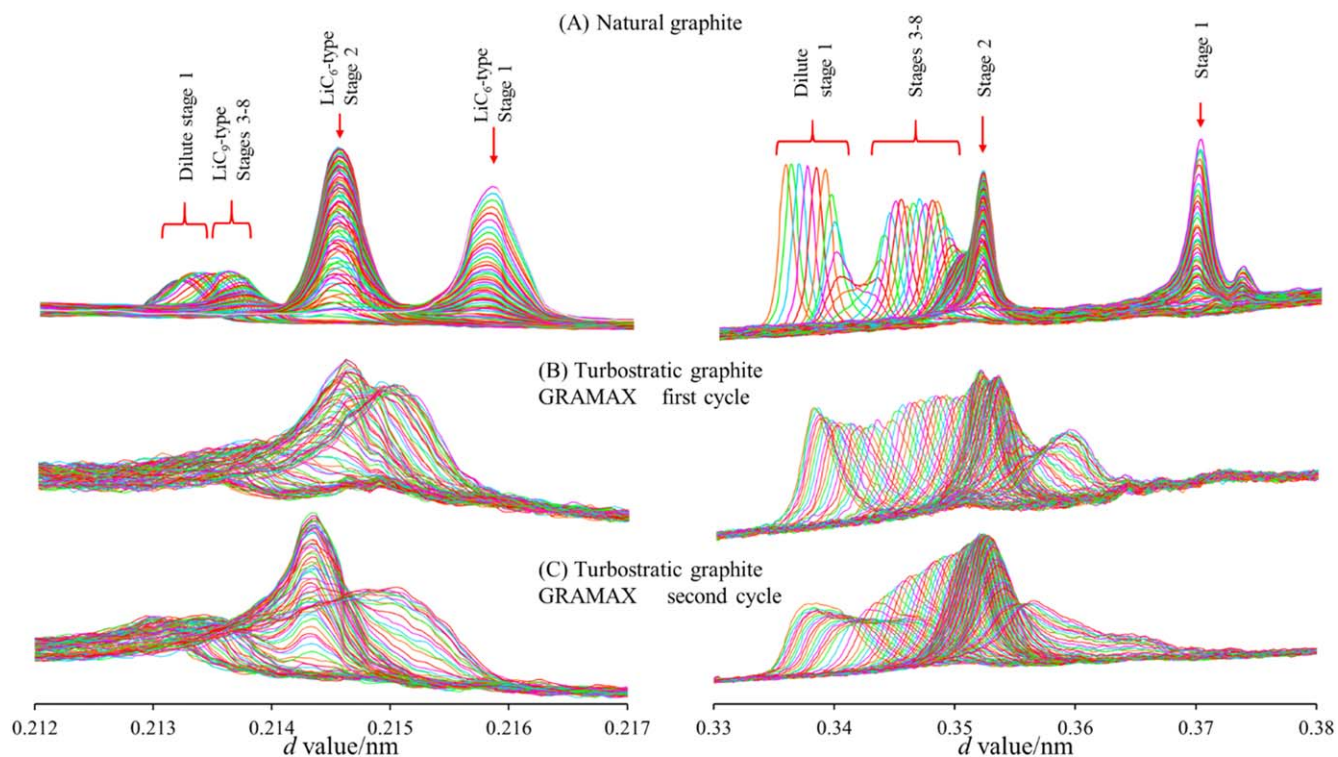


Figure 5. Superimposition of the dynamic changes of the 100 and 002 diffractions of (A) natural graphite and GRAMAX in the (B) first cycle and (C) second cycle every 1% SOC during the charge process.

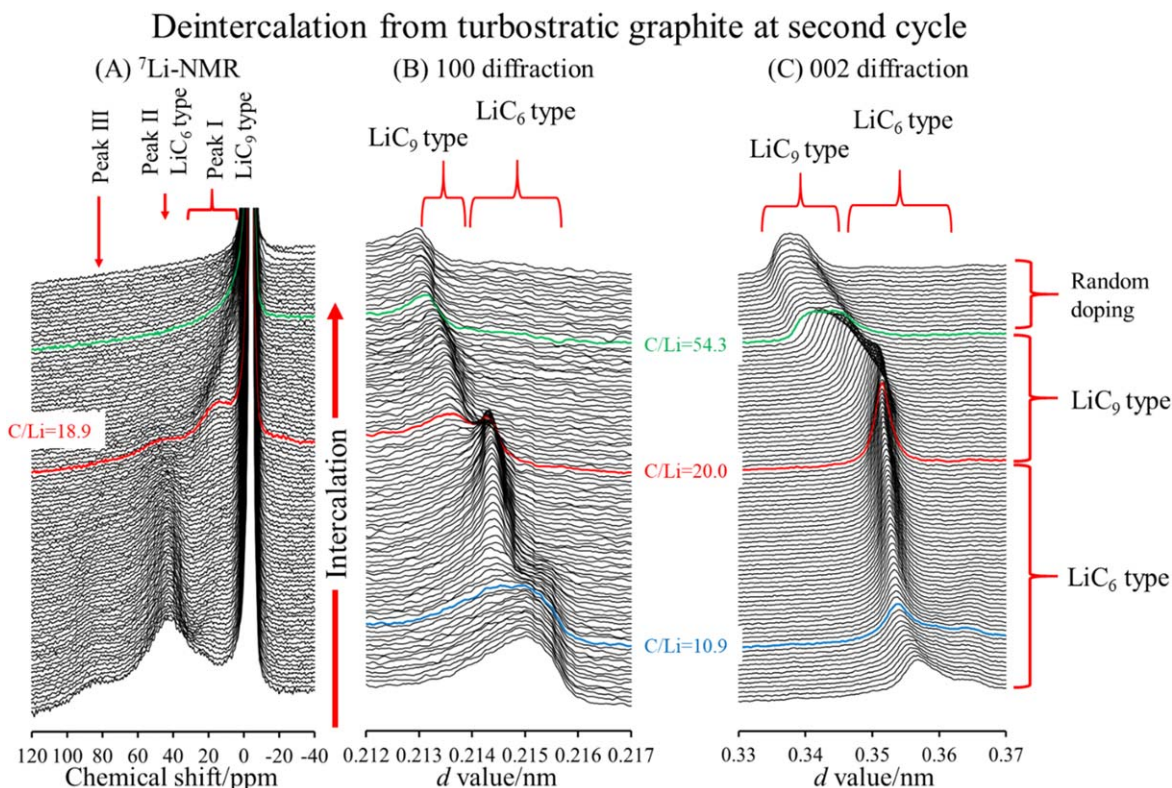


Figure 6. Dynamic changes of the ⁷Li-NMR spectrum and 100, and 002 diffraction profiles of GRAMAX during the discharge (deintercalation) process in the second cycle.

from the LiC₆-type structure to the LiC₉-type structure was also observed in the 100 and 002 diffractions near C/Li = 20. In addition, because there was no clear peak in the ⁷Li-NMR spectrum for C/Li

> 55, it is considered that the LiC₉-type structure disappeared owing to the decrease in the Li-ion concentration, and the Li ions were randomly located in the layer. Furthermore, comparing Figs. 4A and

6B, peak I was more clearly observed during deintercalation compared with during intercalation, indicating that there was clear hysteresis in the process of intercalation/deintercalation.

Estimation of the in-plane structure of Li-intercalated turbostratic graphite.—Generally, a turbostratic graphite such as GRAMAX has a random stacking structure (Fig. 7D) instead of an AB-stacking type structure like natural graphite (Fig. 7A). In such a carbon structure, when the graphene sheets adjacent to each other are misoriented at an angle ϕ , as shown in Fig. 7D, a super lattice called a “rotational moiré pattern” is formed whose periodicity depends on the misorientation angle. As a result, the pseudo AA-type and the pseudo AB-type stacking area are regularly appears in an island shape. The moiré period distance D is expressed by the following equation,

$$D = \frac{a_0}{2 \sin \phi/2} \quad [2]$$

where a_0 is the two-dimensional lattice constant of graphite. The magenta rhombus in the figure is a superlattice formed by the moiré pattern.^{26,27} Since each graphene sheet randomly stacks independently of each other, there is a distribution in the misorientation angle. Therefore, the moiré pattern also changes depending on the misorientation angle between the layers. As already discussed, the LiC_9 and LiC_6 type in-plane structures are formed even in the turbostratic graphite. It is considered that the Li ions are arranged in the interlayers as follows.

In the case of graphite with the AB-stacking structure, such as in natural graphite, intercalation of Li ions causes slipping of the graphene layers, resulting in an AA-stacking structure, which first

forms the LiC_9 -type in-plane structure (Fig. 7B) and then rearranges to form the LiC_6 -type in-plane structure (Fig. 7C). In this case, because an almost perfect LiC_9 - or LiC_6 -type in-plane structure is formed in the layers, all of the Li species have equivalent electronic states, we observe a single signal is the ^7Li -NMR spectrum. However, in the case of turbostratic graphite that forms a moiré pattern in the layers, pseudo-AB- and pseudo-AA-stacking areas form between two adjacent graphene layers, as shown in Fig. 7D. The Li ions are only located in the pseudo-AA-stacking area to form the LiC_9 - (Fig. 7E) or LiC_6 -type (Fig. 7F) in-plane arrangement via random doping state. In this case, the domain size of the formed in-plane structure is smaller than that of natural graphite. That is, it is short-range ordered, so that the line width of the SXD profile causes broadening. In addition, comparing the states of the Li ions located in the central and peripheral parts of the pseudo-AA stacking area, the positional relationship between the upper and lower graphene layers in contact with each Li ion is slightly displaced owing to the degree of misorientation. Hence, the interaction between the Li ions and carbon atoms is different between the center and periphery of the pseudo-AA stacking area. That is, the electronic state of the Li ions changes in a gradient from the central portion to the peripheral portion. As a result, the line width of the signal in the ^7Li -NMR spectrum becomes broad in the case of GRAMAX.

Furthermore, in the case of GRAMAX, because each graphene sheet stacks randomly, each misorientation angle and each center position of the rotational moiré pattern are different. Consequently, when the Li ions intercalate, a periodic in-plane structure is formed in the in-plane direction depending on the size of the moiré pattern. On the other hand, because the periodicity is lost in the c -axis direction by the random stacking, the concept of the stage structure does not hold in a strict sense. The stacking order in the c -axis

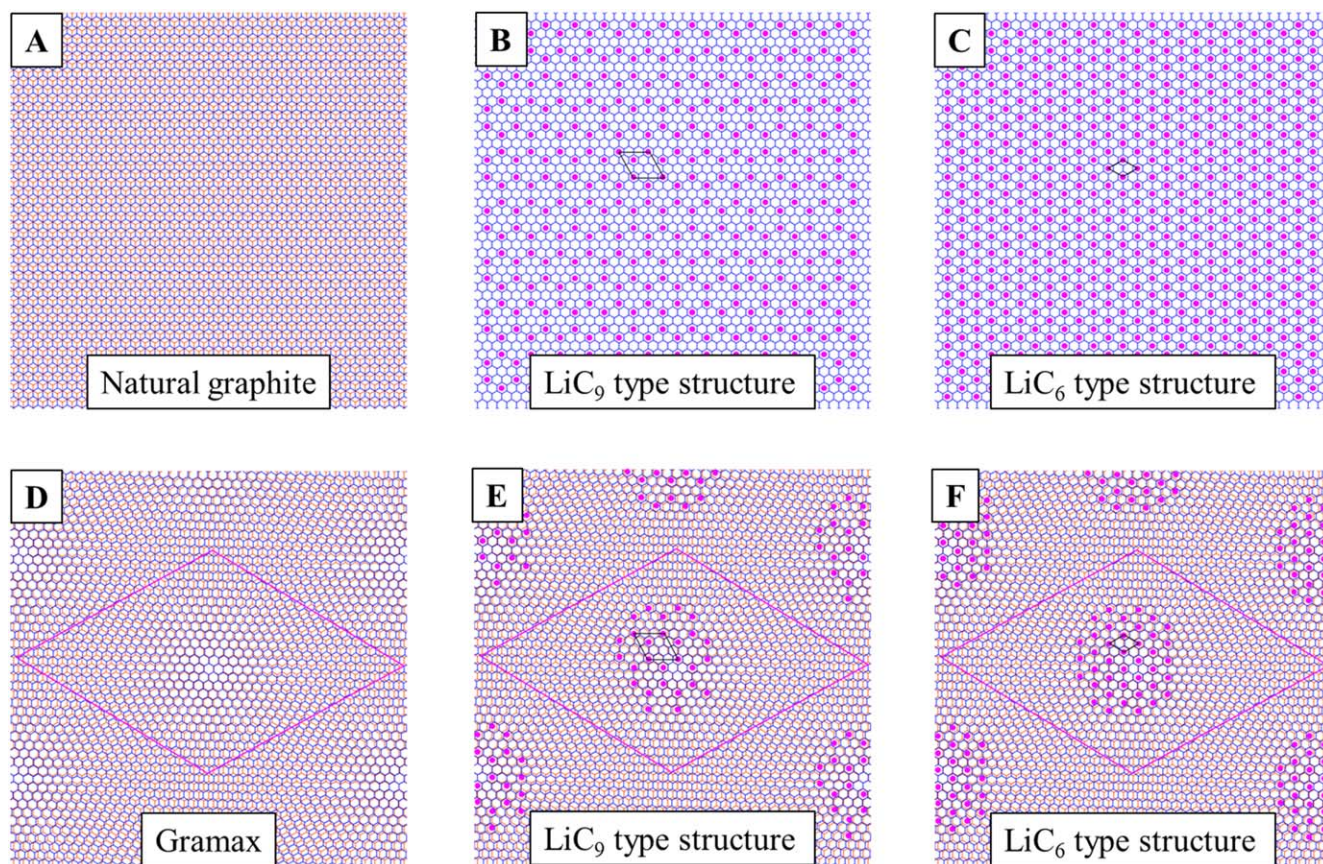


Figure 7. Images of in-plane ordering of the Li species. Magenta rhombus shows the superlattice formed by the rotational moiré pattern by misorientation of two adjacent graphenes, and the black rhombus shows the LiC_9 and LiC_6 type in-plane superlattices. (A) Natural graphite with AB-stacking. (B) Superlattice of LiC_9 type in-plane structure. (C) Superlattice of LiC_6 type in-plane structure. (D) Superlattice composed of the moiré pattern. (E) Pseudo- LiC_9 -type superlattice. (F) Pseudo- LiC_6 -type superlattice.

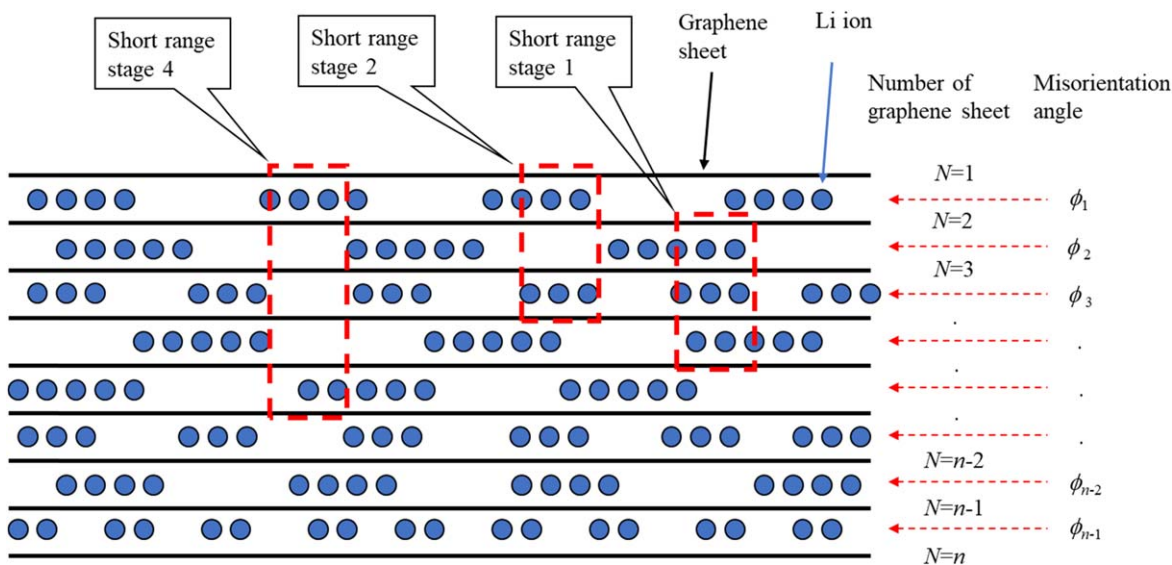


Figure 8. Schematic diagram of the stacking state in turbostratic graphite.

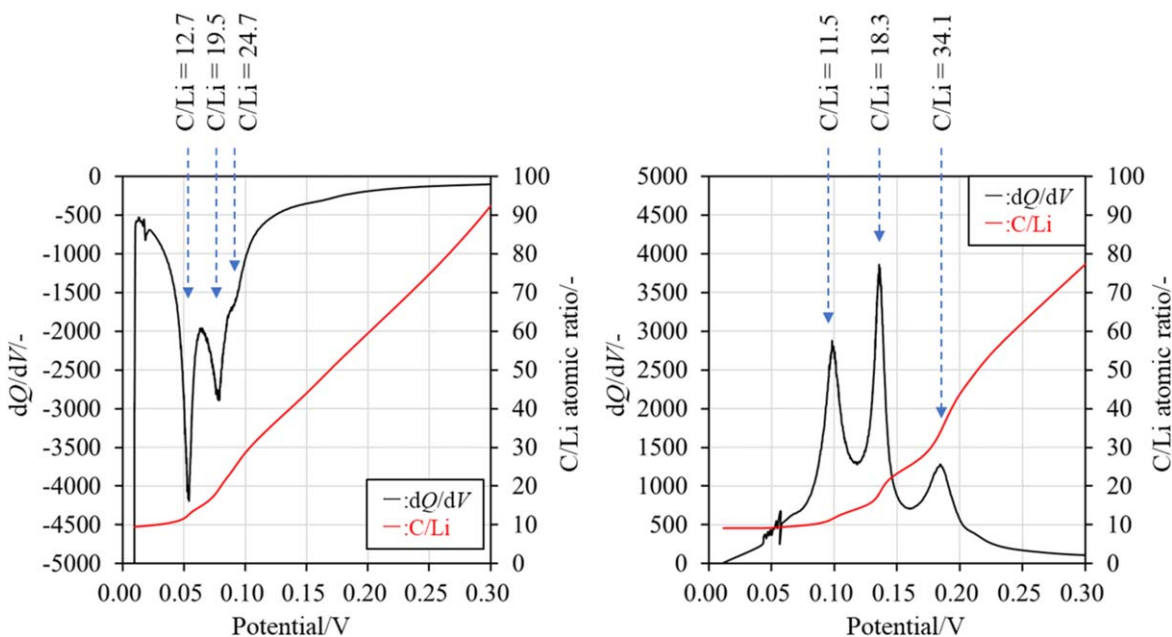


Figure 9. Differential and V - C/Li curves in the second cycle.

direction is very low, and it is presumed that various short-range stage structures form locally as shown in Fig. 8. Therefore, the probability of the formation of continuous pseudo-AA-stacking area at the same position along the c -axis direction is considered to be extremely low, and the structure corresponding to stage 1 is not formed.

V - dQ/dV curve.—The V - dQ/dV and V - C/Li curves estimated from the charge/discharge curves in the second cycle are shown in Fig. 9. During the charge process, three anodic peaks were observed at $C/Li = 24.7$, 19.5 , and 12.7 . Each peak position was in good agreement with the inflection point of the V - C/Li curve, suggesting that there was a clear structural change in the vicinity of this composition. The SXD profile showed a change from the LiC_9 -type in-plane structure to the LiC_6 -type in-plane structure at $C/Li = 24.3$ (Fig. 4). Therefore, the peak of $C/Li = 24.7$ is because of the formation process of the LiC_9 -type structure. In addition, the peaks

of $C/Li = 19.5$ and 12.7 are both located in the region where the LiC_6 -type structure is formed, and the satellite peak derived from the LiC_6 -type structure begins to appear in the 7Li -NMR spectrum at $C/Li = 13.4$. It suggests that these two peaks are because of the formation process of the LiC_6 -type structure accompanying rotation of the graphene layers. However, it is not sufficient to analyze the details from this measurement result.

As in the charge process, in the discharge process, three cathodic peaks were observed at $C/Li = 11.5$, 18.3 , and 34.1 , and the peak positions were also in good agreement with the inflection point positions of the V - C/Li curve. Because the transition from the LiC_6 -type structure to the LiC_9 -type structure was observed at $C/Li = 18.9$ in the dynamic change of the 7Li -NMR spectrum in Fig. 6A, the peak of $C/Li = 34.1$ would be because of deintercalation of Li ions from the LiC_9 -type structure. The peaks of $C/Li = 11.5$ and 18.3 are considered to correspond to the anodic peaks of $C/Li = 19.5$ and 12.7 , but the details are not clear.

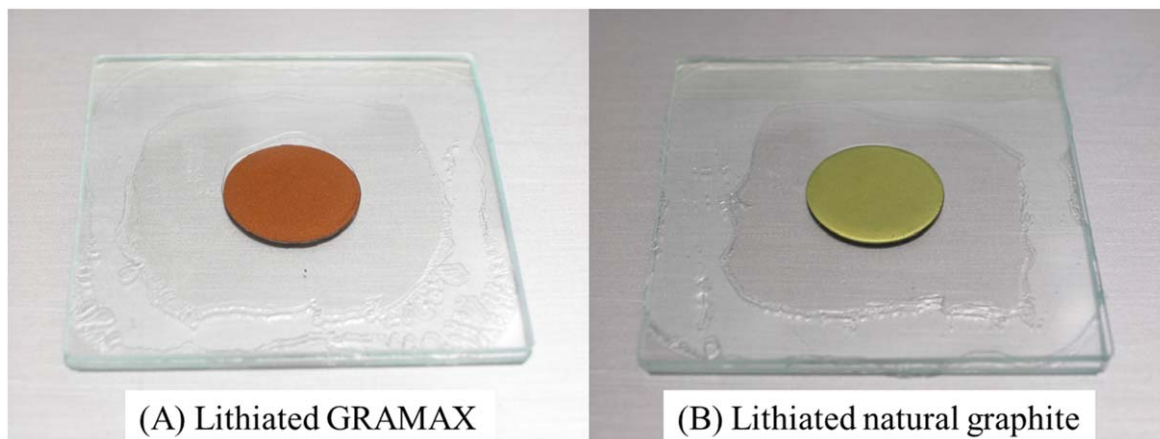


Figure 10. Appearance of the lithiated GRAMAX and natural graphite electrodes.

Appearance of the electrodes.—From the charge/discharge curve in Fig. 1, GRAMAX only exhibited a discharge capacity of 236 Ah kg^{-1} ($\text{LiC}_{8.9}$), which was far lower than the theoretical capacity of graphite of 372 Ah kg^{-1} even when fully charged. The appearance of the GRAMAX and natural graphite electrodes after being fully charged is shown in Fig. 10. The former was orange or metallic bronze and the latter was gold in appearance. The differences in the in-plane structures and saturated compositions of Li ions between GRAMAX and natural graphite cause a difference in the electron-density states on the graphene sheets. As a result, the degrees of visible light absorption of the π -electron systems are different.

Conclusions

The intercalation behavior of Li in turbostratic graphite has been investigated by synchronized operando analysis with ^7Li -NMR and SXD measurements. In the turbostratic graphite structure, a rotational moiré pattern formed by misorientation between two adjacent graphene layers, and a pseudo-AA- and pseudo-AB-stacking structure formed. As a result, LiC_9 -type and LiC_6 -type in-plane structures only formed in the pseudo-AA-stacking area depending on the misorientation angle, as for natural graphite. The domain formed by these in-plane structures was a short-range ordered structure that changed depending on the misorientation angle. It was also found that the graphene layers randomly stacked along the c -axis direction. Thus, a clear stage structure did not form, as in the case of natural graphite.

Acknowledgments

This work is based on results obtained from the project “Research and Development Initiative for Scientific Innovation of New Generation Batteries 2 (RISING2),” JPNP16001, commissioned by the New Energy and Industrial Technology Development Organization (NEDO). The synchrotron X-ray diffraction experiments were performed at the BL28XU beamline of the SPring-8 facility with the approval of the Japan Synchrotron Radiation Research Institute (JASRI) (proposal nos. 2018A7603, 2019A7613, 2019B7613, and 2020A7613). We thank Tim Cooper, PhD, from Edanz (<https://jp.edanz.com/ac>) for editing a draft of this manuscript.

ORCID

Hiroyuki Fujimoto  <https://orcid.org/0000-0003-4562-7715>
Mitsuo Kawasaki  <https://orcid.org/0000-0002-4642-5755>

References

1. N. Sonobe, M. Ishikawa, and T. Iwasaki, *35th Battery Symposium in Japan, Abstr.*, 47 (1994).
2. Y. Liu, J. S. Xue, T. Zheng, and J. R. Dahn, *Carbon*, **34**, 193 (1996).
3. T. Zheng, W. Xing, and J. R. Dahn, *Carbon*, **34**, 1501 (1996).
4. K. Guérin, M. Ménétrier, A. Février-Bouvier, S. Flandrois, B. Simon, and P. Biensan, *Solid State Ionics*, **127**, 187 (2000).
5. K. Gotoh, M. Maeda, A. Nagai, A. Goto, M. Tansho, K. Hashi, T. Shimizu, and H. Ishida, *J. Power Sources*, **162**, 1322 (2006).
6. H. Fujimoto, K. Tokumitsu, A. Mabuchi, N. Chinnasamy, and T. Kasuh, *J. Power Sources*, **195**, 7452 (2010).
7. A. Mabuchi, K. Tokumitsu, H. Fujimoto, and T. Kasuh, *J. Electrochem. Soc.*, **142**, 1041 (1995).
8. K. Tokumitsu, A. Mabuchi, H. Fujimoto, and T. Kasuh, *J. Electrochem. Soc.*, **143**, 2235 (1995).
9. N. Takami, A. Satoh, M. Oguchi, H. Sasaki, and T. Ohsaki, *J. Power Sources*, **68**, 283 (1997).
10. N. Takami, A. Satoh, T. Ohsaki, and M. Kanda, *Electrochim. Acta*, **42**, 2537 (1997).
11. K. Tatsumi, N. Iwashita, H. Sakaebe, H. Shioyama, S. Higuchi, A. Mabuchi, and H. Fujimoto, *J. Electrochem. Soc.*, **142**, 716 (1995).
12. T. Zheng and J. R. Dahn, *Synth. Metals*, **73**, 1 (1995).
13. T. Zheng and J. R. Dahn, *Physical Review B*, **53**, 3061 (1996).
14. Y. Ozaki, N. Tanaka, T. Fujii, H. Fujimoto, and C. Natarajan, *45th Japan Battery Symposium, Abstr.*, **3D02**, 516 (2004).
15. Y. Ozaki and K. Haraguchi, (2006), The 22nd International Battery, Hybrid and Fuel Cell Electric Vehicle Symposium & Exposition (Yokohama).
16. H. Fujimoto, *J. Power Sources*, **195**, 5019 (2010).
17. H. Fujimoto and K. Morita, *Carbon*, **56**, 317 (2013).
18. N. Kambe, M. S. Dresselhaus, G. Dresselhaus, S. Basu, A. R. McGhie, and J. E. Fischer, *Mat. Sci. Eng.*, **40**, 1 (1979).
19. D. Gerard, M. Chaabouni, P. Lagrange, M. E. Makrini, and A. Hérol, *Carbon*, **18**, 257 (1980).
20. M. S. Dresselhaus and G. Dresselhaus, *Adv. Phys.*, **30**, 139 (1981).
21. D. Billaud, E. McRae, J. F. Mareche, and A. Hérol, *Synth. Met.*, **3**, 21 (1981).
22. H. Fujimoto, H. Kiuchi, S. Takagi, K. Shimoda, K. Okazaki, Z. Ogumi, and T. Abe, *J. Electrochem. Soc.*, **168**, 040509 (2021).
23. H. Fujimoto, M. Murakami, T. Yamanaka, K. Shimoda, H. Kiuchi, Z. Ogumi, and T. Abe, *J. Electrochem. Soc.*, **168**, 080508 (2021).
24. M. Letellier, F. Chevallier, and M. Morcrette, *Carbon*, **45**, 1025 (2007).
25. F. Chevallier, F. Poli, B. Montigny, and M. Letellier, *Carbon*, **61**, 140 (2013).
26. H. Saadaoui, J. C. Roux, and S. Flandrois, *Carbon*, **31**, 481 (1993).
27. M. Endo, K. Oshida, K. Kobori, K. Takeuchi, K. Takahashi, and M. S. Dresselhaus, *J. Mater. Res.*, **10**, 1461 (1995).